Top Organomet Chem (2005) 16: 117–149
DOI 10.1007/b138075

Published online: 10 September 2005

Spectroscopic Characterization of Organometallic Centers on Insulator Single Crystal Surfaces: From Metal Carbonyls to Ziegler–Natta Catalysts

T. Risse (✉) · H.-J. Freund

Fritz-Haber-Institut der Max-Planck Gesellschaft, Abteilung Chemische Physik, Faradayweg 4–6, 14195 Berlin, Germany
risse@fhi-berlin.mpg.de

Abstract A detailed knowledge of the microscopic properties is one of the prerequisites for an understanding of heterogeneous catalysts. A strategy which has proven to be valuable in this respect is the use of model systems prepared under well-defined conditions and a subsequent characterization of these systems under both ultrahigh vacuum as well as ambient pressures. In the following review we focus on two systems where organometallic species play an important role. The first class of systems under consideration is metal carbonyls prepared under ultrahigh vacuum conditions. In particular, we will discuss the prospects of these species for use as probes for the environment of the deposited metal atom. In the second part we will discuss experiments on Ziegler–Natta model catalysts. In particular, we will describe how surface science studies of these systems can help to elucidate atomistic properties of surface sites involved in polymerization reactions.

Keywords Oxide surfaces · Metal carbonyls · Ziegler–Natta catalyst · IR spectroscopy · EPR spectroscopy

Abbreviations
CESR Conduction band electron spin resonance
ESR Electron spin resonance
EPR Electron paramagnetic resonance

ISS Ion scattering spectroscopy
IRAS Infrared absorption spectroscopy
1 L (Langmuir) = 10^{-6} Torr s
LEED Low energy electron diffraction
LRI Laser reflection interferometry
ML Monolayer
NMR Nuclear magnetic resonance
STM Scanning tunneling microscopy
TMA Trimethylaluminum
TEA Triethylaluminum
TPD Temperature programmed desorption
XPS X-ray photoelectron spectroscopy

1 Introduction

A common property of working heterogeneous catalysts is their complexity with respect to structure, chemical stoichiometry, and reaction kinetics [1]. This complexity often hampers a detailed microscopic understanding of the systems due to a lack of appropriate methodology. Therefore, strong efforts have been made to develop model systems which retain some degrees of complexity of real systems and investigate their influence on the catalytic properties of system under both ideal ultrahigh vacuum conditions, as well as ambient pressures [2–8]. One strategy, which might be classified as a bottom-up approach, is to prepare model catalysts starting from an ideal single crystal surface, under well-defined ultrahigh vacuum conditions. From this starting point, reaction centers are added to the surface in a controlled manner. A variety of methods are employed to prepare reactive centers, depending on the nature of the catalytic site. For the preparation of deposited metal particles, an important class of heterogeneous catalysts, atomic vapor deposition or cluster beam methods are used, which may be considered physical methods (e.g., [9–13]). On the other hand, grafting of catalytically active sites can be achieved by specific reactions of organometallic compounds with functional groups on the surface, ultimately aiming at a single-site catalyst (e.g., [14]).

In the following review we will focus on two classes of systems: dispersed metal particles on oxide supports as used for a large variety of catalytic reactions and a model Ziegler–Natta catalyst for low pressure olefin polymerization. The discussion of the first system will focus on the characterization of the environment of deposited metal atoms. To this end, we will discuss the prospects of metal carbonyls, which may be formed during the reaction of metal deposits with a CO gas phase, as probes for mapping the environment of deposited metal atoms [15–19].

The second part of the review will describe results on a model Ziegler–Natta catalyst [20, 21]. This investigation was inspired by the pioneering work of the Somorjai group [22], who have investigated these systems with a variety of surface science methods [23]. This review is not meant to survey the current state of knowledge in heterogeneous Ziegler–Natta catalysis. Instead, we will focus on experiments performed on model systems prepared under well-defined ultrahigh vacuum conditions and review the current state of knowledge based on these results.

2 Metal Carbonyls on a Well Defined Alumina Surface

Small supported metal particles may exhibit properties fundamentally different from the corresponding bulk materials (e.g., [24, 25]). This becomes increasingly important for decreasing particle sizes. For such particles the geometric structure, their electronic properties, and their reactivity are closely correlated. In fact, it has been shown that even changes in the size of the particles by a single atom may alter their properties drastically [12, 26]. The situation may be complicated further by the fact that different structural isomers and/or different interactions of deposited atoms with the substrate may change the catalytic properties of a particle of given size considerably. Therefore, a detailed knowledge of the environment of a deposited atom, e.g., its nucleation site or its coordination is a prerequisite for a comprehensive understanding of the deposition system. However, gathering this kind of detailed information is still challenging even for well-defined model systems. In this context, vibrational properties of metal carbonyls can give additional insight into the environment of deposited atoms.

In the present study we have used a thin, well-ordered atomically flat alumina film grown on a NiAl(110) single crystal surface as a model support [27]. The atomic arrangement within line defects of this film have recently been investigated [28]. In addition, there exists a proposed structure of the film based on X-ray diffraction data which is controversially debated at the moment [29]. The structure and size of the oxide-supported metal particles were controlled utilizing nucleation and growth of vapor deposited metal atoms under ultrahigh vacuum conditions.

In previous work on nucleation and growth of a variety of metals on this alumina film, three different nucleation sites were identified:

(i) Line defects, which show the strongest interaction with metal atoms. These are most notably antiphase domain boundaries with a characteristic distance of 100–200 Å, whose structure has recently been investigated in detail by low temperature scanning tunneling microcopy (STM) [28]. Reflection domain boundaries and substrate steps also have to be considered [30, 31].

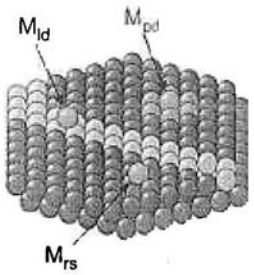

Fig. 1 Schematic representation of the different nucleation sites on the alumina film: M_{ld} nucleation at line defects, M_{pd} nucleation at point defects, M_{rs} nucleation at regular surface sites

(ii) Point defects [16, 32], which have a number density of about 10^{13} cm^{-2}.
(iii) Regular oxide sites, which exert the weakest interaction on metal atoms [16].

The adsorption sites are schematically shown in Fig. 1. However, it should be emphasized at this point that this is a schematic picture. The precise atomic positions for these species are not known at present.

The nucleation behavior of transition metal particles is determined by the ratio between the thermal energy of the diffusing atoms and the interaction of the metal atoms at the various nucleation sites. To create very small particles or even single atoms, low temperatures and metal exposures have to be used. The metal was deposited as metal atoms impinging on the surface. The metal exposure is given as the thickness (in monolayer ML) of a hypothetical, uniform, close-packed metal layer. The interaction strength of the metals discussed here was found to rise in the series from Pd < Rh < Co (≈ Ir) < V [17, 32]. Whereas Pd and Rh nucleate preferentially at line defects at 300 K and decorate the point defects at 90 K, point defects are the predominant nucleation center for Co and V at 300 K. At 60 K, Rh nucleates at surface sites between point defects [16, 33].

In the following we shall see that a more detailed picture of the structural properties of small metal deposits and their electronic interaction with the substrate can be obtained from the infrared spectra of metal carbonyls created in situ by reaction with CO from the gas phase.

2.1
Small Metal Particles and Single Metal Atoms

Figure 2 shows infrared spectra (IR or IRAS) of low Pd, Rh, and V exposures at a sample temperature of 60 K (Rh, Pd) and 90 K (V) with respect to the CO dosage [15, 17]. The spectra in the CO stretching region are characterized

by broad bands as well as very narrow peaks with a half width below 4 cm^{-1}. First, we will discuss the results obtained for Rh particles, and afterwards move on to the results for V and Pd.

At low CO dosage a small amount of rhodium deposited at 60 K shows two bands at 2000/1994 and 1966 cm^{-1} (see Fig. 2a). With increasing CO coverage a new peak at 2116 cm^{-1} evolves. Later, additional bands appear at 2172, 2087, and around 2037 cm^{-1}. While the latter signals grow in, the peak at 1966 cm^{-1} vanishes. With increasing coverage the oscillator strength around 2000 cm^{-1} is redistributed in a complicated manner. However, at saturation the spectrum simplifies again, and a single line at 1999 cm^{-1} is observed. Despite the large number of lines in the spectrum it is important to emphasize that the small line width of the peaks at constant frequency indicates structurally uniform, well-defined surface species containing only few CO ligands.

The situation becomes less complicated in case of Rh deposition at 90 K. For low coverage only one peak at 1994 cm^{-1} is observed while at high coverage (see Fig. 3a) a broad band centered around 2075 cm^{-1} and a sharp, prominent peak at 2117 cm^{-1}, also observed at 60 K, is found [15]. In addition, the spectrum shows a sharp band of lower intensity at 2097 cm^{-1}. Since all bands are located above 1950 cm^{-1} the CO molecules are predominantly bound terminally in all cases. The broad line, which changes somewhat in shape upon annealing to 300 K (see Fig. 3a), is due to CO on larger Rh particles [33, 34] in line with observations on technical catalysts [35–40].

The band at 1994 cm^{-1}, observed at low CO coverage, was assigned to a monocarbonyl Rh(CO) species. The nature of the species observed at 2117 cm^{-1} has been elucidated using mixtures of different CO isotopes. As shown in Fig. 4, the band splits into three bands after adsorption of ^{12}CO/^{13}CO mixtures proving the presence of a dicarbonyl species

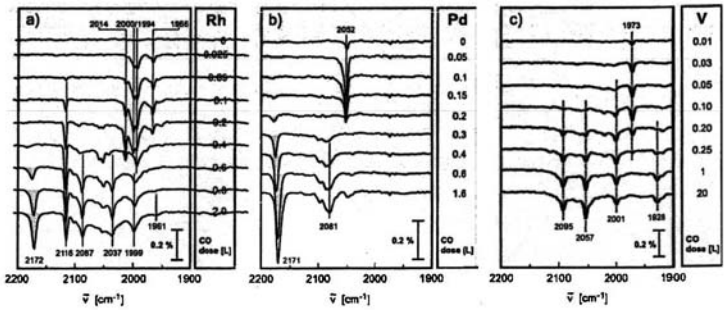

Fig. 2 Infrared spectra taken after metal deposition and exposure to increasing amounts of CO at a constant temperature: **a** 0.02 ML Rh, 60 K; **b** 0.013 ML Pd, 60 K; **c** 0.2 ML V, 90 K. CO bands present on nominally clean surfaces are due to CO adsorption from the background during sample preparation

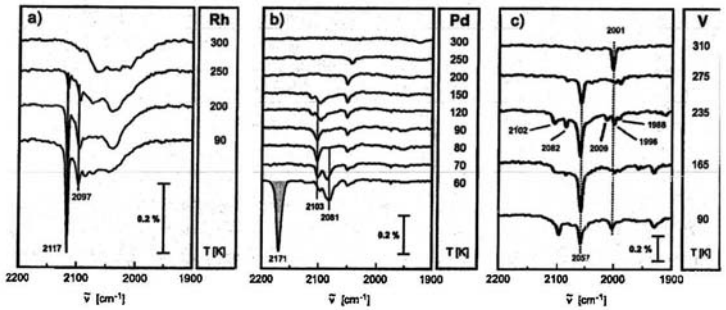

Fig. 3 Infrared spectra taken after metal deposition and CO saturation as a function of substrate temperature: **a** 0.024 ML Rh, T_{dep} = 90 K; **b** 0.013 ML Pd, T_{dep} = 60 K; **c** 0.2 ML V, T_{dep} = 90 K

$Rh(CO)_2$ [16]. Such a dicarbonyl should possess two vibration modes. However, only the symmetric mode is observable in the IR spectrum. The asymmetric mode is inaccessible to an IR experiment on a metal surface due to the so-called metal surface selection rule, which prohibits the observation of dipole excitation if the transition dipole moment is oriented parallel to the surface. It should be noted that the observed frequencies fit well to values observed for $Rh(CO)_2$ on technical Rh/Al_2O_3 catalysts [35–40] ($\sim 2100\ cm^{-1}$) and $Rh(CO)_2$ on planar $TiO_2(110)$ surfaces [41] ($2112\ cm^{-1}$).

From combination with IR results at room temperature and STM investigations it was concluded that the dicarbonyls are located at point defects of

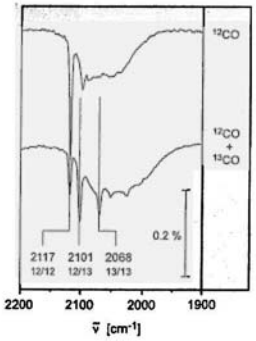

Fig. 4 Infrared spectra taken after deposition of 0.028 ML of Rh at 90 K and subsequent saturation with CO. *Top* pure ^{12}CO; *bottom* approximately equimolar mixture of ^{12}CO and ^{13}CO

the alumina film [16]. Hence, the species are formed directly from a heterogeneously nucleated Rh atom at this defect site. The species are fairly stable and start to decompose above 200 K as indicated in Fig. 3a.

The band at 2172 cm^{-1} observed in spectrum of the 60 K deposit is remarkably different from the others in the sense that it is blue shifted with respect to the gas phase value of CO (2143 cm^{-1}). This peak can be attributed to CO adsorption on the alumina film [27].

In comparison to the 90 K situation, two additional peaks at 2000 and 1966 cm^{-1} were found. Due to the reduced diffusion length of the metal atoms at lower temperatures the new peaks should be due to monocarbonyls attached to the additionally populated sites. Therefore, both species were tentatively assigned to monocarbonyls at "regular" oxide sites [15]. Investigations of the electronic structure of single Pd atoms on this surface have shown that a large variety of different adsorption sites exist, which leads to considerably different electronic structures of adsorbed Pd atoms as probed by scanning tunneling spectroscopy [42]. Thus, it is conceivable to propose metal carbonyls with different stretching frequencies nucleated at sites that were classified as "regular" adsorption sites based on their population with respect to temperature.

The intensity of the dicarbonyl at 2116 cm^{-1} is considerably reduced as compared to the 90 K deposit, indicating that the amount of metal atoms trapped at point defects is reduced for growth at 60 K. The difference in the nucleation sites is also reflected by the lower thermal stability of the systems, which decompose between 80 and 150 K as compared to 200 to 250 K for the 90 K deposits. With isotope mixing experiments the peak at 2087 cm^{-1} was assigned to a carbonyl with three or more CO ligands, while the peak at 1999 cm^{-1} is associated to a monocarbonyl [32].

It is remarkable that the feature at 2097 cm^{-1} which was observed for a preparation at 90 K is missing at 60 K. The peak shows the characteristics of a monocarbonyl in mixing experiments. Furthermore, thermal treatment of the deposit as shown in Fig. 3a reveals a slightly increased thermal stability of this species as compared to the dicarbonyl at point defects. From this information it was suggested that the monocarbonyl is located at line defects of the alumina film [15].

Moving now from Rh to Pd, the IR spectrum of Pd deposits at 60 K exhibits a single narrow line at 2052 cm^{-1} in the low CO coverage regime as shown in Fig. 2b [15]. With increasing coverage a signal at 2081 cm^{-1} grows, accompanied by the peak at 2171 cm^{-1} associated with CO adsorption on the alumina film. This behavior is markedly different to the behavior observed at 90 K where stretching features due to on-top bound CO(μ^1 – CO) at 2098 cm^{-1} and multiply coordinated molecules ($\sim 1940\ cm^{-1}$) are observed [15]. These broad signals with a large fraction of on-top bound CO are typical for adsorption on small, disordered Pd particles as observed on technical catalysts [43–45], as well as on corresponding model systems [46].

For vanadium deposits the IR spectrum (Fig. 2c) taken after saturation at 90 K is characterized by four peaks at 2095, 2057, 2001, and 1928 cm^{-1} [17]. However, at low CO dosage a single vibration at 1973 cm^{-1} is observed that first gains intensity with increasing CO amounts and vanishes for saturation coverage. It is important to note that the IR spectra of vanadium grown at 300 K are also characterized by several sharp lines indicative of well-defined surface species [17]. This is in contrast to Rh and Pd deposits, which show only broad lines characteristic for adsorbates on larger metal particles [33, 47, 48]. It is a consequence of the enhanced metal-support interaction of vanadium, which reduces the diffusion length of adatoms considerably. The two bands at 2057 and 2001 cm^{-1} observed at 90 K are also present at 300 K. However, the spectrum taken at 300 K shows several additional bands at 2116, 2034, 2019, and 1988 cm^{-1}, which are missing in the spectra of the 90 K deposits. This is remarkable since the overall morphology, as probed by STM, is essentially independent of the preparation temperature [17]. Upon annealing, the peak at 2057 cm^{-1} quickly grows at the expense of most of the other species (see Fig. 3c). In the course of the treatment new features develop. Two of them are close to species observed for 300 K deposits. Interestingly, the species at 2001 cm^{-1} is the most stable species for this preparation condition, while for the deposits prepared at 300 K the band at 2034 cm^{-1}, missing for the 90 K deposits, is the most stable species. The latter band is the one being observed exclusively for small CO doses at 300 K.

Due to the complexity of the spectra the use of isotopic CO mixtures does not allow an unambiguous determination of the stoichiometry. However, some of the features can be prepared such that the interference with other spectral components is negligible. From these experiments it was possible to assign the peak at 2057 cm^{-1} to a tricarbonyl $V(CO)_3$ and the one at 2001 cm^{-1} to a dicarbonyl $V(CO)_2$. In addition, the two peaks observed at low coverage, namely at 1973 cm^{-1} observed at 90 K and at 2034 cm^{-1} observed at 300 K, were assigned to monocabonyls V(CO) [17]. A summary of the different stoichiometries, corresponding stretching frequencies and nucleation sites is given in Table 1.

The frequencies of the carbonyl species anchored to oxide surfaces are blue shifted with respect to their matrix isolated counterparts. The main reason for these frequency shifts are charge-transfer processes between the metal center and the oxide support. This interaction modifies the extent of metal-to-CO-π-back-donation [49]. Andrews et al. were among the first to use the correlation between charge and IR frequency to measure the charge state of the metal carbonyl [50]. However, one has to include the partial charge localized at the metal center to establish the proper charge-frequency correlation [51]. It is therefore necessary to correct for the difference between the charge state of the whole carbonyl and the charge at the metal center. In addition, the geometry as well as the electronic state of the carbonyl influences the stretching frequency considerably (e.g., [52]). In order to correlate these

Table 1 Stoichiometry and corresponding IR stretching frequencies of different metal carbonyls. Charges for monocarbonyls were estimated from the correlation between IR stretching frequency and charge of the metal center as inferred from theoretical calculations (for details see [15, 17])

	T [K]	$\tilde{\nu}$ [cm^{-1}]	Charge	Adsorption site
RhCO/alumina	90 K	1994	-0.2 *to* $+0.2$	Point defects
	60 K	2097	0.6 *to* $+0.7$	Line defects
	60 K	2000/1966	-0.3 *to* $+0.2$	Regular surface sites
$Rh(CO)_2$/alumina	90 K, 60 K	2117	-	Not known
PdCO/alumina	60 K	2052	~ 0	Point defects
VCO/alumina	90 K	1973	$+0.2$	Regular surface sites
	300 K	2034	$+0.5$	Point defects
$V(CO)_2$/alumina	90 K, 300 K	2001	-	Not known
$V(CO)_3$/alumina	90 K, 300 K	2057	-	Not known
VCO/silica	90 K	2016	$+0.3$ *to* $+0.4$	Not known

quantities, precise values of the stretching frequency mostly taken from data acquired in Ne matrices and ab-initio calculations are needed for the ground state as well as for both charged states. For the cases studied so far almost linear charge frequency relations have been found [15, 17], although it should be kept in mind that these values can only serve as estimates for the charge of the metal center.

From these linear relationships the charges of the two V(CO) carbonyls at 1973 cm^{-1} and 2034 cm^{-1} were determined to be $+0.2$ and $+0.5$ electrons. The positive sign means that electrons are transferred from the carbonyl to the substrate. The corresponding charges for Rh(CO) located around 2000 cm^{-1} is close to zero between -0.2 and $+0.2$ electrons. However, the monocarbonyl at 2097 cm^{-1}, which was tentatively assigned to a monocarbonyl at a line defect, shows a significant charge of about $+0.6 - +0.7$ electrons. This value fits well with one measured for vanadium at 300 K. Yet, it is not clear why the two vanadium monocarbonyls observed at different temperatures show such distinctly different stretching frequencies.

Two different explanations may be given to account for this behavior:

(i) The two types of monocarbonyls are located at different sites of the alumina support. In this case the degree of charge transfer must depend on the nucleation site.

(ii) The carbonyls nucleated at the same site for both temperatures. However, the charge transfer between substrate and carbonyl is a function of the temperature. For example, an activated process which would be more effective at 300 K than at 90 K may explain this behavior.

It was possible to discriminate between the two situations by an experiment at intermediate temperature. At 120 K both species, the one at 2037 cm^{-1} (together with its ^{13}CO counterpart at 1988 cm^{-1}) and the one at 1973 cm^{-1} with its ^{13}CO satellite, were observed simultaneously. This proves that the first explanation is correct, indicating the variation of the metal support interaction for the various nucleation sites [17].

Despite the uncertainties regarding the absolute values of the charge transfer the following conclusions can be drawn:

(i) The extent of charge transfer depends on the metal nucleation site. It is larger for adsorption on point defects as compared to regular terrace sites. The metal to oxide charge transfer is also theoretically predicted for regular terrace sites [53]. The situation is much more complex for adsorption on defect sites such as anion vacancies. The result depends on the charge of the vacancy, and opposite effects are expected, e.g., for singly positive charge (F^+) and neutral (F^0) oxygen vacancies, usually called color centers because of their optical absorption in the visible [12, 54–56].

(ii) The extent of charge transfer depends on the reactivity of the metal towards oxygen. Rh monocarbonyls prepared at 90 K have been shown to nucleate at point defects, yet they are almost neutral whereas the corresponding vanadium particles seem to be charged. The latter result is confirmed by XPS (X-ray photoelectron spectroscopy) and XAS (X-ray absorption spectroscopy) [17].

Finally, it is interesting to note that the carbonyl chemistry can be tuned to some extent by the choice of the substrate under consideration. Figure 5 shows the IR spectra of CO adsorbed to 0.03 ML of vanadium deposited at 90 K to a well-ordered silica film [17]. At low CO coverage a single sharp line at 2016 cm^{-1}, most probably due to a monocarbonyl, is observed which is transformed into another sharp feature at 2075 cm^{-1}. The latter is tentatively assigned to a higher carbonyl $V(CO)_x$ with $x \geq 2$. However, most of the IR intensity is located in the broad feature from 1900–2200 cm^{-1}, which is due to CO molecules adsorbed to larger vanadium particles. This is distinctly different to the alumina case where sharp narrow lines indicative of well-defined carbonyl species dominate the spectrum even at 300 K. It can be interpreted as a smaller metal support interaction which results in an increased diffusion length of the atoms on the surface. However, the position of the signal at 2016 cm^{-1}, which is associated with a monocarbonyl species, points towards a charge transfer from the carbonyl to the surface by approximately (+)0.3–0.4 electrons. This is in line with the observation on the alumina surface, but the relative amount of these sites is distinctly smaller on silica than on alumina. This indicates that not only the reactivity of the metal towards oxygen, but also the chemistry of the substrate surface, is very important for the properties of the deposited metal particles. In the future we need to explore the chemistry of these single site systems.

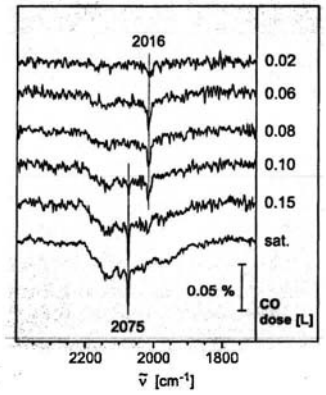

Fig. 5 Infrared spectra of 0.03 ML vanadium deposited on silica as a function of CO exposure. Preparation and measurements were done at 90 K

2.2 Carbonyl Species on Metal Particles

We have shown in the preceding section that the IR spectra of well-defined metal carbonyls provide valuable information of the environment of the deposited metal atom. However, IR signals of CO molecules adsorbed on larger particles suffer from broad lines, which hamper a more detailed analysis of the data. In the forthcoming section we will present results on cobalt particles where carbonyl species are formed on larger particles containing hundreds of atoms.

Figure 6 shows IR spectra of CO adsorbed at 44 K on Co particles grown on the alumina film at 300 K [19]. An average thickness of 1 ML Co was deposited, which corresponds to a mean particle diameter of ~ 1.6 nm (170 atoms). At low coverage, an absorption band appears at 1967 cm^{-1}, attributable to atop-bound CO [57]; this peak gradually shifts to higher energy with increasing coverage. Just after the adsorption band at 1967 cm^{-1} forms, another band at 2060 cm^{-1} also begins to grow in intensity; this second feature shifts only slightly to 2068 cm^{-1} at saturation coverage and is much stronger than the band due to atop-bound CO(μ^1 – CO) at this point. As the absorption band due to atop adsorption shifts to higher energy, it melds into a tail of the absorption feature at 2068 cm^{-1}, making it difficult to quantify the stretching frequency for atop-bound CO at the saturation limit. After annealing to 300 K, the peak attributable to atop-bound CO remains at about 2000 cm^{-1} and the feature at 2068 cm^{-1} vanishes (data not shown).

The adsorption band at 2068 cm^{-1} has no counterpart on surfaces of smooth single crystals. There, only red shifted bands (1900–1967 cm^{-1}) were

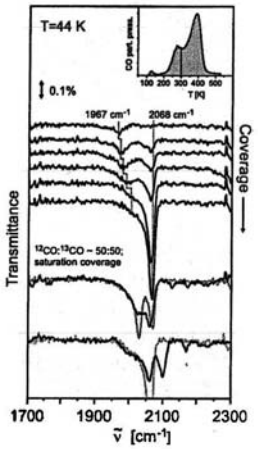

Fig. 6 IR spectra of adsorbed CO on 1 ML Co deposited at room temperature on the alumina film as a function of CO coverage. Spectra were taken at 44 K. *Black trace second up from the bottom* shows the spectrum resulting from saturation coverage of a 50 : 50 mixture of ^{13}CO : ^{12}CO. *Overlaid gray trace* is artificially created by adding the saturation coverage spectra ^{12}CO and ^{13}CO scaled by a factor 1/2. *Lowest black trace* shows the spectrum of CO saturation coverage on particles grown by 1 MLCo + 0.05 MLPd. *Corresponding grey trace* is the pure Co spectrum for comparison. *Right inset* shows TPD spectrum of 1 ML Co [64]

observed which have been assigned to bridge bound (μ^2 – CO) species [57, 58]. Adsorption bands at 2080 cm^{-1} and 2040 cm^{-1} have been observed for CO adsorbed on sputtered Co(0001) [58] and un-annealed films [59]; in the former case this was attributed to CO adsorption at defect sites [58], and in the latter case it was attributed to carbonyl formation [59]. An adsorption band near 2068 cm^{-1} has also been observed on supported Co particles [60–62], and has been attributed to an $M(CO)_n$ species [60]. The assignment as a single-centered carbonyl is based on analogy with metal carbonyls, which suggests the following categorizations [63]: on-top (μ^1 – CO) 2000–2130 cm^{-1}, twofold bridge (μ^2 – CO) 1860–2000 cm^{-1}, and threefold bridge (μ^3 – CO) 1800–1920 cm^{-1}. Given these categories, it seems reasonable to attribute the band at 2068 cm^{-1} to a $M(CO)_n$ species. However, as compared to the sharp signals observed for carbonyls formed on single atoms the band seen here is rather broad. This is in line with expectations due to the much more heterogeneous environment in such particles.

The stoichiometry of the compound was investigated by isotope exchange experiments along the lines described in the preceding section. The pure

Scheme 1

^{13}CO case shows a peak at 2022 cm^{-1}, as expected from simple mass consideration. It is evident from the spectrum of an equimolar mixture of ^{13}CO and ^{12}CO at saturation coverage (shown as the black trace in the second to bottom panel of Fig. 6) that the species responsible for this band consists of strongly coupled oscillators (the light trace, second to bottom panel of Fig. 6 visualized the expectation for a decoupled system). From a careful analysis of combined annealing and isotope exchange experiments it was concluded that the observed intensity pattern is due to the formation of cobalt carbonyls $Co(CO)_x$ with $x \geq 3$ [19]. The formation of a carbonyl species is further corroborated by the intensity behavior of the system. A quantitative evaluation of the IR intensities in correlation with the corresponding TPD results (see inset Fig. 6) reveals a dynamic dipole moment of the species at 2068 cm^{-1}, being at least a factor of two higher than for the regular on-top sites [18]. In combination with theoretical calculations, it could be shown that this intensity enhancement of the carbonyl species is due to a decoupling of the CO bond to a low coordinated metal from those atoms embedded in the metal surface. Such species can only exist on metal atoms with a low metal–metal coordination based on simple chemical considerations. Thus, IR intensity, rather than the position of the band, might be a more reliable reporter on the chemical nature of the species.

The presence of a site with a low metal–metal coordination is compatible with the non-crystalline nature of the cobalt deposits [64]. It is to be expected that these sites exhibit different chemical reactivity than the usual adsorption sites. This can be verified by subsequent deposition of a small amount (0.1 Å) of Pd atoms, which are known to nucleate exclusively on the cobalt particles [64]. The corresponding IR spectrum is shown as the bottom trace in Fig. 6. It is seen that an additional peak appears at 2105 cm^{-1}, which is readily assigned to CO bound terminally to Pd. More importantly, the growth of this Pd feature is completely at the expense of the carbonyl species, indicating that Pd nucleates almost exclusively at these low coordinated sites and prevents the formation of the carbonyl species.

In summary, we have shown that metal carbonyls formed in situ by adsorption of CO under ultrahigh vacuum condition can serve as a very sensitive tool for monitoring the nucleation site as well as the environment of the metal atom. It was shown that low coordinated metal atoms, in particular

single atoms, show distinct chemical properties that depend upon the metal and may be altered by the substrate. The specific reactivity of low coordinated sites being present on small metal particles was demonstrated by subsequent evaporation of a second metal that exclusively decorates this adsorption site.

3
Ziegler–Natta Model Catalyst

The polymerization of α-olefins with so-called Ziegler–Natta catalysts is one of the most important industrial processes based on an organometallic catalyst. Since the early work by Ziegler [65] and Natta [66, 67] transition metal (in particular titanium) halides and organoaluminum compounds have been used [68, 69]. The development of industrial processes has increased the activity and efficiency of the catalysts by orders of magnitudes as compared to the first generation of (homogeneous) Ziegler–Natta catalysts [69]. One breakthrough in the development of more efficient catalysts was achieved by the so-called third generation of Ziegler–Natta catalysts introduced in the mid 1970s. These systems represent supported catalysts where inorganic chlorides, such as $MgCl_2$ and $CoCl_2$ are used as supports to increase the amount of active Ti [70]. The high activity of these catalysts has allowed use of low catalyst concentrations and, therefore, catalyst residues can remain in the polymer [69]. The literature on "classical" Ziegler–Natta catalysis is huge (e.g., [69, 71–79] and references therein). In addition, new developments such as metallocenes/methylaluminoxane catalysts have recently increased the interest in this field substantially [68, 80].

Despite this large body of work most of the experimental characterization of supported third generation Ziegler–Natta catalysts has been indirectly done via polymer product analysis. However, as has been frequently stated in the literature [69, 71–79], knowledge of surface properties of such systems is of fundamental importance to describe the process and its mechanism in detail. Recently, theoretical studies have given interesting and important contributions to our understanding of the surface sites (e.g., [81–84]). From an experimental point of view, surface science studies of model systems can offer a valuable strategy for investigating the nature of the active surface species. However, such studies on polymerization catalysts have been rather scarce. Model studies on the Phillips catalyst have been performed [85, 86] and more importantly, Somorjai and coworkers [22, 23, 87–91] have developed model systems for supported Ziegler–Natta catalysts, which allow a characterization of surface species in the course of the preparation. The procedure is sketched in Fig. 7, which may also serve as an outline for the forthcoming sections.

First, we will briefly discuss the growth properties of epitaxially grown $MgCl_2$ films used as support for the Ti centers. $TiCl_4$ was anchored on these

substrates as the active component. The anchoring process has been studied by several techniques including electron spectroscopy [89] and, recently in our group, by electron spin resonance (ESR) spectroscopy. It will be shown that surface defects in the $MgCl_2$ film are crucial in this process. The subsequent activation of the catalyst by adding a co-catalyst, namely an alkyl aluminum compound (trimethylaluminum, TMA, or triethylaluminum ,TEA) lowers the oxidation state of Ti (e.g., [23]). It will be shown how EPR spectroscopy as an in-situ technique can be used to elucidate the mechanism of the activation step. Finally, the polymerization of ethylene and propylene was monitored using several techniques such as IR spectroscopy, Raman spectroscopy or laser reflectance interferometry (LRI).

3.1
$MgCl_2$ Thin Film as a Model Support

$MgCl_2$ is used as support for heterogeneous Ziegler–Natta catalysts, therefore preparation of a well-defined epitaxial $MgCl_2$ film is an important prerequisite for the subsequent steps of the preparation procedure. $MgCl_2$ films were grown on a variety of different metal surfaces. Among them polycrystalline Au, and single crystalline Pd(111), Pd(100), Pt(111), and Rh(111) were

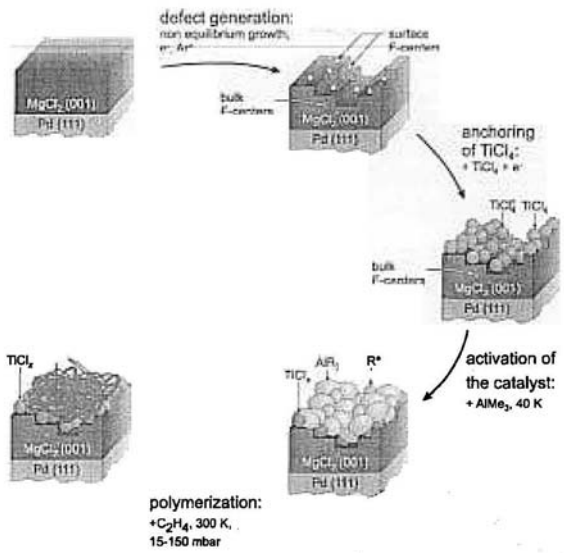

Fig. 7 Schematic representation of the preparation of a Ziegler–Natta model catalyst

used [21, 88, 92–94]. $MgCl_2$ was thermally evaporated under ultrahigh vacuum conditions as molecular $MgCl_2$ [92]. Thick films grown on Pt(111) and Pd(111) at elevated temperatures (610–630 K) show a hexagonal LEED pattern of a $MgCl_2$ film as shown in Fig. 8c. Due to the small escape depth of low energy electrons the diffraction pattern is purely determined by diffraction spots of the $MgCl_2$ film. The size of the unit cell was determined to be 3.6–3.7 Å, consistent with the unit cell parameters of α-$MgCl_2$ grown along the (001) direction. A quantitative analysis of the LEED spot intensity as a function of the electron energy (I–V analysis) (e.g., [95–97]) confirms the formation of films with α-$MgCl_2$ structure [94]. In the monolayer regime a (4×4) superstructure is observed by LEED (Fig. 8b). Such a film can be prepared either by heating the multilayer film above the multilayer desorption temperature at 680 K or by preparation of the film around 700–710 K [21, 93]. The term monolayer refers here to a Cl – Mg – Cl trilayer with a height of nominally 5.9 Å. For this thickness the diffraction experiment will probe both the film as well as the substrate, therefore the (4×4) pattern is due to the 4 : 3 coincidence of substrate and adsorbate lattice as schematically shown in Fig. 8d. It is clear that, even though the surface is polar, the system is stable due to the $MgCl_2$ structure, which is a case B structure according to Tasker's rules [98]. Analysis of the temperature programmed desorption experiments reveals an activation energy for $MgCl_2$ desorption of 224 kJ/mol for several single crystal surfaces [93], which is in good agreement with the heat of sublimation of bulk magnesium chloride, 238 kJ/mol [99]. A similar value (201 kJ/mol) was observed for $MgCl_2$ films on polycrystalline gold [88].

The growth direction of $MgCl_2$ is independent of the substrate symmetry [93]. Growth on a cubic crystal, namely Pd(100), leads to hexagonal LEED pattern. However, the structure of the films is much more complex due to the

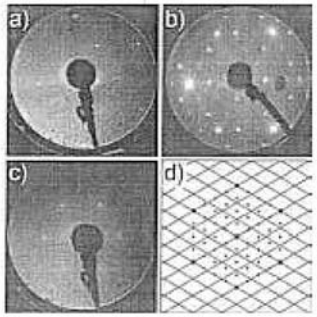

Fig. 8 LEED pattern as observed during preparation of a $MgCl_2$-film. **a** Pd(111), **b** 1 ML $MgCl_2$(001)/Pd(111), **c** multilayer $MgCl_2$(001)/Pd(111). **d** Schematic real space representation of **b**; the *mesh* represents the Cl lattice and *spots* the underlying Pd lattice

existence of symmetry equivalent rotation domains that give rise to 12 LEED spots on top of a ring of diffuse intensity, indicating a strong perturbation of the structure [93]. This is a direct consequence of the layered structure of the $MgCl_2$ and surface energies of surfaces other than (001) [100].

It is important to study whether the prepared $MgCl_2$ film exhibits pinholes. This can be done by temperature programmed desorption experiments of probe molecules. On Pd, CO is a suitable probe. The only signals observed are in the range of 70 K, which is compatible with desorption from the $MgCl_2$ film [21]. There were no signals in the range where CO desorbs from Pd(111) [101]. The same result was achieved by Magni and coworkers for $MgCl_2$ films on gold using *n*-hexane as a probe molecule [88].

3.2
Adsorption of $TiCl_4$

On a well-ordered $MgCl_2$ film prepared at high temperatures $TiCl_4$ does not adsorb at 300 K. This result is independent of the substrate used, namely it was found for gold as well as palladium substrates [21, 88]. $TiCl_4$ can of course be condensed on the surface at low temperatures, but by elevating the temperature all $TiCl_4$ desorbs well below room temperature. Magni and Somorjai in their $TiCl_4$ pioneering work had already realized the necessity of producing defects in the film to bind the $TiCl_4$ precursor [22]. The idea goes back even further (e.g., [102, 103]), however. Early on it was noted that low coordinated edge and corner sites on $MgCl_2$ crystallites serve as binding sites for $TiCl_4$ [68, 70, 104]. Recent model calculations strongly support this picture [81–84, 105].

Several routes have been used to produce defect sites on $MgCl_2$ surfaces: One way is to grow the $MgCl_2$ film at low temperatures so that the mobility of the $MgCl_2$ is too low to allow for the formation of a fully epitaxial film. However, a major problem of this procedure is the tendency to produce films containing pinholes, which change the reactivity of the system [21]. Another option is to bombard the surface either with electrons or ions [22, 87–90, 106, 107].

How do these treatments change the structure of the surface? Growth of the film at lower temperatures leads to more diffuse LEED spots, indicating a higher degree of disorder on the surface. This is corroborated by the fact that these films exhibit a sharp EPR signal at $g = 2.004$ as shown in Fig. 9a, which indicates the formation of paramagnetic chlorine vacancies in these films. This is in contrast to a film grown at elevated temperatures which is free of paramagnetic resonance signals.

Starting from a stoichiometric, well-ordered $MgCl_2$ film, an increasing dosage of sputtered ions leads to increasing background intensity of the LEED picture, which finally results in a complete loss of all diffraction spots [108]. Even though the process removes material from the surface, the surface

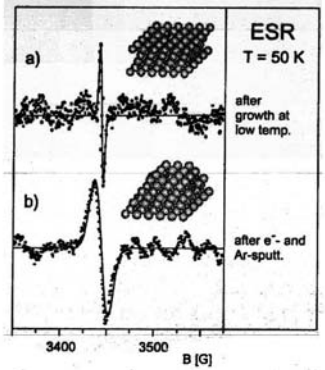

Fig. 9 EPR spectra of color center in $MgCl_2$ films for two different preparation conditions: **a** film grown at lower temperature; **b** initially well-ordered film after bombardment with electrons and argon ions

composition remains almost constant [106]. In contrast, electron bombardment leads to an electron-stimulated desorption of chlorine atoms from the surface. For low dosage this results in the formation of chlorine vacancies. Higher electron dosages reduce the $MgCl_2$ further and the formation of metallic magnesium could be observed by electron spectroscopy [106]. It should be noted that the surface of the film is always chlorine terminated, as revealed by ion scattering spectroscopy (ISS), indicating that metallic magnesium tend to diffuse to the metal substrate interface [106]. However, neither of these two processes alone is sufficient to produce paramagnetic defects on the surface. Subsequent argon ion bombardment (150 eV, 1 $\mu A/cm^2$, 3 min) of a sample initially exposed to electrons does produce an EPR signal, as shown in Fig. 9b. As compared to the spectra created by growth at lower temperatures, the signal is shifted slightly to higher g-value ($g = 2.007$). Additionally, an increase of the line width from 4 G to 14 G is observed.

Obviously, only parts of the defects created on the surface are paramagnetic, and thus EPR active. Nonetheless subsequent $TiCl_4$ deposition on samples covered with a non-epitaxial $MgCl_2$ film quenches the EPR signal by 40% [21]. This can be taken as a clear indication that some of the defects are localized on the surface of the $MgCl_2$ film, while most of the defects are bulk defects not influenced by adsorbed $TiCl_4$.

What is the nature of the defects seen in the EPR spectra? For alkali and alkali earth halogenides it is well known that irradiation with X-ray, neutrons, gamma-radiation, or electrons produce paramagnetic color centers (F-center) [109–111]. If these centers are created in large amounts, they can be stabilized by the formation of metal clusters as observed for $MgCl_2$ films after prolonged electron radiation [106]. From the temperature dependence

as well as the intensity of the signal it was concluded that the signal is due to the presence of color centers. The difference in line width between the two preparation procedures (4 versus 14 G) might be explained by the dependence of the g-values on the local coordination of the low coordinated sites. Thus, the more defected sample should show a broader line due to an increased heterogeneity of the defect sites. A schematic view of the situation is shown as insets in Fig. 9.

$TiCl_4$ was exposed to the surfaces by vapor deposition under electron bombardment on the surface. After this procedure Ti was found on the surface. Detailed analysis of the adsorbed Ti species by XPS measurements have shown that Ti exists as Ti^{2+} and Ti^{4+}. However, Ti^{3+} centers were not observed using XPS [87]. EPR spectroscopy offers the possibility to test this result, because Ti^{3+} as a d^1 system is a paramagnetic system. Thus, it should be EPR active, at least in its monomeric form. Figure 10 shows two distinctly different EPR spectra attributed to Ti^{3+} species which have been observed after deposition of $TiCl_4$ to differently prepared samples. The relatively sharp signal b ($\Delta H_{pp} = 14$ G) centered at $g = 1.96$ was observed after deposition of $TiCl_4$ in the presence of electrons on a surface free of paramagnetic defects, followed by subsequent electron bombardment. It should be noted that systems not exposed to additional electrons after deposition of the $TiCl_4$ lack this signal. This is in line with the observations by Magni who found only Ti^{2+} and Ti^{4+} for electron-assisted deposition of $TiCl_4$ [87]. However, further electron irradiation leads to electron-stimulated desorption of chlorine, which results in a reduction of Ti^{4+} centers to Ti^{3+}. The XPS spectrum observed after this treatment showed an increase of the Ti^{2+} species at the expense of the Ti^{4+} lines. In addition, the spectral features broadened, which can be due to an additional Ti^{3+} component. However, Magni et al. did not interpret the

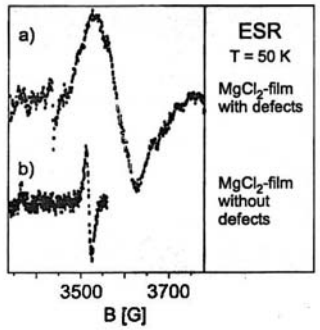

Fig. 10 EPR spectra of Ti^{3+} centers at 40 K after electron stimulated $TiCl_4$ deposition and subsequent electron bombardment. *Top* defective $MgCl_2$ film; *bottom* defect-free $MgCl_2$ film

broadening at this point due to the lack of an independent verification for the presence of Ti^{3+} species.

Upon aluminum alkyl exposure the intensity of the EPR signals is reduced by 10–60% depending on the preparation condition. This can be interpreted as a further reduction of the Ti^{3+} centers in agreement with other experiments (see next section); however, the surface concentration of these sites varies considerably with preparation conditions.

The other signal shown in Fig. 10a was observed after adsorption of $TiCl_4$ under electron bombardment and subsequent treatment with electrons on $MgCl_2$ substrates, which show paramagnetic defect states. In this case the signal intensity is increased by more than an order of magnitude as compared to the former case. In addition, the signal is shifted up-field, now located at $g = 1.93$, with a peak-to-peak width of 50–90 G, depending on the preparation.

The g-values found are situated among values reported for $TiCl_3$ in octahedral ($g = 1.94$) and tetrahedral ($g = 1.96$) environments [112–114]. These values were found for Ziegler–Natta catalysts. While the signal observed on the less defected surface is close to the value observed for tetrahedral environments, the signal of the surface showing paramagnetic defects is centered at the value for octahedral environments. Comparing the line width of the signals measured here with the ones in the literature, the general trend of the signal at $g = 1.94$ to be broader than those at $g = 1.96$ also holds true for these measurements; however, the line width of the resonance at $g = 1.93$ is considerably broader than in the literature. Considering the stronger disorder of these systems it is more likely that isolated Ti^{3+} centers are formed in this case, which may comprise different local environments. The increase in line width would thus be caused by inhomogeneous line broadening.

However, there is no indication that the presence of the observed signals correlates with the polymerization efficiency of the catalyst. In fact, systems which exhibit these signals are less effective catalysts and in some cases do not even polymerize ethylene under the chosen conditions. In contrast, systems without EPR signals correlated to Ti^{3+} species are found to be catalytically active. It has to be emphasized at this point that the lack of an ESR signal associated to Ti^{3+} ions, in cases where no additional argon or electron bombardment has been applied, cannot be interpreted as an indication of the absence of Ti^{3+} centers at the surface. It has been discussed in the literature that small spin-lattice-relaxation times, dipole coupling, and super exchange may leave a very small fraction of Ti^{3+} that is detectable in an EPR experiment [115, 116]. From a combination of XPS and EPR results it unlikely that Ti^{3+} centers play an important role in the catalytic activity of the catalysts.

A second class of catalysts was prepared by deposition of $TiCl_4$ and Mg metal on gold surfaces [91, 117]. Mg deposition and subsequent $TiCl_4$ exposure results in a complex structure with Mg metal being located at the gold interface and covered by a $MgCl_2$ layer. On top of that $TiCl_x$ species of different oxidation states were found. In contrast to deposition on the $MgCl_2$ films, not only Ti^{4+} and Ti^{2+} but also Ti^{3+} centers were found under these preparation conditions. However, the ratio of the different oxidation states changes significantly with the preparation condition [91, 117]. For simultaneous deposition of $TiCl_4$ and Mg the situation is different. In this case Mg is completely oxidized to $MgCl_2$. The $MgCl_2$ film is covered by $TiCl_x$ species of different oxidation states. Similar to the sequential deposition, all three oxidations are present and the precise composition depends on the relative concentration of $TiCl_4$ and Mg atoms at the surface during growth [91]. Mesitylene (1,3,5 trimethyl-benzene) was used as a probe molecule to titrate different adsorption sites on these systems. The mesitylene TPD from these films are characterized by two desorption peaks around 200 K and 250 K. The desorption temperatures are virtually identical to the ones observed on the pure $MgCl_2$ film. This was attributed to the fact that both systems are chorine terminated, thus the adsorption energy is mostly determined by the local configuration of chlorine atoms, which was considered to be similar for both cases. The two peaks were assigned to mesitylene desorbing from coordinatively saturated sites at 200 K and desorption from low coordinated sites or defect sites at 250 K [118].

A third class of catalysts was prepared by electron beam induced deposition of $TiCl_4$ on a polycrystalline Au foil. Deposition of $TiCl_4$ at 300 K leads to films which comprise Ti^{4+} and Ti^{2+} species as inferred from XPS measurements [90]. Depending on the experimental parameters (background pressure of $TiCl_4$, electron flux, electron energy) different composition of Ti oxidation states are observed [23]. From angular-dependent measurements it was concluded that the Ti^{4+} centers are more prominent at the surface of the titanium chloride film, while the Ti^{2+} centers are located in the bulk [90].

Temperature-programmed desorption of mesitylene shows a marked difference to the catalysts prepared on $MgCl_2$ surfaces. The spectrum contains only one desorption peak at around 250 K. Due to the similar desorption temperature to the peak observed for $MgCl_2$-based films, this peak was assigned to desorption from low coordinated or defect sites [118].

3.3
Activation of the Catalyst

Activation of the catalyst is usually performed by exposure to a co-catalyst, namely an aluminum alkyl. The model catalysts were successfully activated by trimethylaluminum (TMA) and triethylaluminum (TEA), commonly used for this purpose. The compounds were dosed from the gas phase either at room temperature for a prolonged time or for a much shorter time at a surface temperature of 40 K. Nominal 3400 L of TMA or TEA were exposed at room temperature. The chemical integrity of the co-catalyst was verified by IR spectroscopy of condensed films grown at low temperature on the substrates. The spectra were typical for condensed and matrix isolated species [119].

Figure 11a shows a typical ESR spectrum after deposition of TMA on the $TiCl_4/MgCl_2/Pd(1111)$ system at 50 K [20]. The $TiCl_4/MgCl_2$ system was prepared by subsequent deposition of $TiCl_4$ onto an epitaxial $MgCl_2$ film. The intensity of the observed signal scales with the amount of Ti on the surface, which suggests that the observed signal is due to a surface reaction of the TMA with the Ti centers on the surface. This interpretation is corroborated by the fact that the intensity of the EPR signal saturates for increasing dosage of TMA. Additionally, adsorption of TMA on smooth as well as defected $MgCl_2$ gives no signal.

According to XPS investigations by the Somorjai group, interaction of TEA with Ti centers grafted on $MgCl_2$ leads to a reduction of Ti^{4+} center to Ti^{2+} [107]. No indications for the formation of Ti^{3+} centers were found. As indicated in the preceding section, the amount of Ti^{3+} centers present after deposition depends on the preparation conditions. However, for all situations investigated the amount of Ti^{3+} is slightly reduced by the activation process [118, 120]. The mesitylene desorption temperature from the low coordinated sites is reduced by about 15 K whereas the desorption temperature from the regular sites at 200 K is virtually unchanged (small reduction by 2–5 K depending on the preparation) [118]. Thus, it can be concluded that the alkylation takes place at the low coordinated sites. The situation is less obvious for the regular sites due to the small changes observed there.

The EPR spectrum shows, in accordance with the XPS results, no feature that can be attributed to Ti^{3+} centers. What is the nature of the radical observed in the EPR spectrum? It might be thought that methyl radicals are the most natural products in the reduction of a mixed titanium-chlorine-methyl species according to the following simple reaction scheme:

$$AlMe_3 + TiCl_4 \rightarrow AlMe_2Cl + TiCl_3Me \quad (1a)$$

$$TiCl_3Me \rightarrow TiCl_3 + Me^{\cdot} \quad (1b)$$

However, a comparison of the line shape of the observed spectra with spectra of methyl radicals (Fig. 11b) clearly proves that the species present here are not methyl radicals. The EPR spectrum of a methyl radical is a quartet of lines. However, the observed spectrum, though dominated by a quartet structure, shows a couple of additional lines pointing to additional interactions of the unpaired electron. By comparing the observed line shape to other alkyl radicals it turned out that the present spectrum can be attributed to ethyl radicals. Figure 11c shows the EPR spectrum of ethyl radicals created in an ethylchloride matrix generated by photolysis for comparison [121].

How have the C_2H_5 radicals been created?

It has already been shown above that the radicals are most probably produced at the TMA – $TiCl_4/MgCl_2$ interface, where an alkylation of the $TiCl_4$ by ligand exchange is supposed to happen (see reaction scheme above). Assuming this ligand exchange occurs, the primary radical would be a methyl

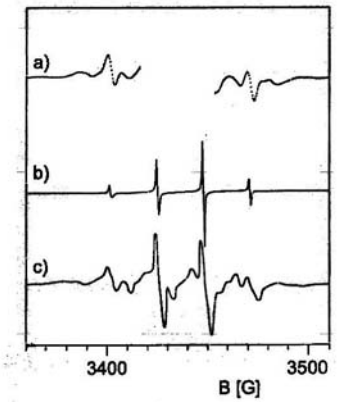

Fig. 11 *a* EPR spectrum of the model catalyst after adsorption of TMA at 50 K; *b* EPR spectrum of methyl radicals [151]; *c* EPR spectrum of ethyl radicals [121]

radical. Methyl radicals have a high mobility, even at low temperature, in the solid state, which makes consecutive reactions likely [122]. A simple reaction yielding ethyl radicals is:

$$CH_3^{\cdot} + Al(CH_3)_3 \rightarrow H_3C - H_2C^{\cdot} + AlH(CH_3)_2 \quad (2)$$

Even though this reaction has not been reported in the literature so far, it can be crudely estimated that it is energetically possible. An alternative reaction may be proposed by analogy to the known chemistry of titanocenes. Here reaction of $Cp_2TiCl_2(Cp = \eta^5 - C_5H_5)$ with $AlMe_3$ yields the Tebbe reagent $Cp_2Ti(\mu^2 - Cl)(\mu^2 - CH_2)AlMe_2$, which is a protected methylidene carbene [123]. It is possible that an analogous surface complex $Ti_S(\mu^2 - Cl)(\mu^2 - CH_2)AlMe_2$ may serve as a source of methylidene to produce ethyl radicals.

The EPR intensity of the ethyl radicals is irreversibly attenuated above 50 K and falls below the detection limit above 80 K. This can be explained by assuming the ethyl radicals to diffuse and recombine at these temperatures, as has been observed for methyl radicals above 45 K [124] and for NO_2 radicals on an oxide surface above 75 K [125].

At 300 K TMA has desorbed from the surface. However, carbon is found on the surface indicating a successful alkylation of the $TiCl_4$. Exposure of the surface to 3400 L at room temperature leads to a similar amount of carbon. This is in contrast to observations by Magni et al. who report on a minimal dosage of 10 000 L to observe carbon on the surface [107]. It is important to note that additional dosage of TMA at low temperature does not produce further radical signals. However, removing the reacted $TiCl_x$ moieties from the

surface, e.g., by soft argon sputtering, and redosing with TMA creates new C_2H_5 radicals, as observed by their EPR spectrum.

A different behavior is observed if TMA is replaced by TEA. Even though the final catalysts are equally active for ethylene polymerization, radicals have never been observed. This is in line with expectations based on indirect evidence [126–128] proposing a disproportionation reaction for the activation with TEA according to:

$$AlEt_3 + TiCl_4 \rightarrow AlEt_2Cl + TiCl_3Et \quad (3a)$$

$$2TiCl_3Et \rightarrow 2TiCl_3 + C_2H_4 + C_2H_6 \quad (3b)$$

Because ethyl radicals have been observed in the preceding experiment, which also suggest that these radicals are stable at 50 K, the initial formation of ethyl radicals would undoubtedly lead to the observation of the radicals. A possible mechanism may be proposed by analogy to molecular organometallic chemistry. Negishi et al. have shown that the reaction of zirconocene dichloride with $AlEt_3$ liberates ethane and forms a coordinated ethylene according to [129]:

$$Cp_2ZrCl_2 + AlEt_3$$

$$\leftrightarrow (Cp_2Zr(Cl)(\mu^2 - Cl)(\mu^2 - Et)AlEt_2 \leftrightarrow Cp_2Zr(Et)(\mu^2 - Cl)_2AlEt_2) \quad (4a)$$

$$Cp_2ZrCl_2 + 2AlEt_3$$

$$\rightarrow Cp_2Zr(\mu^2 - Cl)(\mu^2 - \eta^2 - C_2H_4)AlEt_2 + EtH + Et_2AlCl \quad (4b)$$

Thus it seems possible that analogous titanium-based complexes play a role in the activation of the catalyst with $AlEt_3$ according to:

$$Ti_SCl_2 + AlEt_3$$

$$\leftrightarrow (Ti_S(Cl)(\mu^2 - Cl)(\mu^2 - Et)AlEt_2 \leftrightarrow Ti_S(Et)(\mu^2 - Cl)_2AlEt_2) \quad (5a)$$

$$Ti_SCl_2 + 2AlEt_3$$

$$\rightarrow Ti_S(\mu^2 - Cl)(\mu^2 - \eta^2 - C_2H_4)AlEt_2 + EtH + Et_2AlCl \quad (5b)$$

It should be emphasized that no spectroscopic evidence exists for either of the proposed species; however, the lack of an EPR signal can be taken as strong evidence that no radicals are produced during activation of the catalyst with $AlEt_3$, thus favoring a kind of disproportionation mechanism.

3.4
Polymerization of Ethylene and Propylene

The model catalysts prepared according to the above-mentioned procedures were active for ethylene and propylene polymerization without additional cocatalyst present in the gas phase [21, 23]. The $TiCl_x/MgCl_2$-based catalysts have been proven catalytically active at 300 K and an ethylene pressure above

15 mbar. The polymer films have been characterized by a variety of methods including XPS, IRAS, LRI, and Raman spectroscopy.

We have used IRAS to investigate the polymerization of ethylene on a $TiCl_x/MgCl_2$/Pd(111) catalyst activated with TEA or TMA. The catalysts were exposed at 300 K to 15–150 mbar ethylene. Polyethylene is produced on this catalyst, as shown by the IR spectrum in Fig. 12. Characteristic vibrations are the stretching modes at 2852/2924 cm^{-1}, the doublet of the deformation modes at 1473/1463 cm^{-1}, and the split rocking modes at 730/720 cm^{-1} (see Table 2). The observed frequencies of the stretching modes are situated at positions that indicate a large percentage of *trans* configurations [130–132]. This was taken as an indication that the polymer chains have long range order in *trans* configurations but also contain some *gauche* defects. Similar results were also obtained in other work. Polyethylene formed via diazo methane reactions on Au(111) films showed similar behavior [131]. Also, n-$C_{44}H_{90}$ adsorbed on Au surfaces yielded analogous results. Here the authors found *gauche* defects only in the second layer, while the first represented a flat lying chain [133].

This analysis is corroborated by the signature of the bands in the fingerprint and low frequency regime. A sharp doublet of the scissoring mode at 1473/1463 cm^{-1} is indicative for crystalline polyethylene, while a broad resonance at 1468 cm^{-1} is found for amorphous polyethylene [134–137]. The doublet is caused by a Davidov splitting due to the presence of two polyethylene chains in the unit cell [133, 138]. In this case the relative small half width of the two peaks is a good indication for a rather well-developed crystallinity. Another feature typical for crystalline polyethylene is a doublet in the region of the rocking mode at 730/720 cm^{-1} [135]. In addition, bands in the region between 1300 and 1380 cm^{-1}, which have been observed for disordered polyethylene, are not present these samples [134]. A lower limit for the chain length of the polymer can be estimated from the fact that vibrations in the

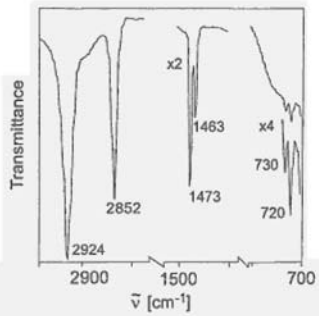

Fig. 12 Infrared spectrum of polyethylene film grown on the model catalyst

Table 2 Comparison of IR frequencies between the model catalyst and data for literature as well as the assignment of the frequencies taken from the literature

ν_{obs} [cm^{-1}]	ν_{ref} [cm^{-1}]	Assignment
2924	2922–2926 Without 2915–2920	CH_2 asymmetric stretching mode d^-: crystalline PE with gauche-defect [131, 133, 146]
2852	2852–2856 Without 2846–2850	CH_2 symmetric stretching mode d^+: crystalline PE with gauche-defect [131, 133, 146, 147]
1473	1470–1473	CH_2 deformation mode orthorombic PE *a*-axis [136, 137, 146–148]
1463	1463	CH_2 deformation mode orthorombic PE *b*-axis [136, 137, 146–148]
730	730–731	CH_2 rocking mode orthorombic PE *a*-axis [135, 149]
720	720	CH_2 rocking mode orthorombic PE *b*-axis [135, 149, 150]

range between 720 and 1300 cm^{-1} are completely missing. For alkanes with a chain length above 20 units the vibrations in this frequency range become so broad that they cannot be observed, which renders this value the lower limit of the chain length in our case [133, 139, 140]. In addition, the line corresponding to terminal methyl groups is very small, which serves as another hint for the polymeric nature of the material produced. It is important to notice that the absence of a line in an IRAS experiment performed under grazing incidence on a metal surface might be due to the so-called metal surface selection rule.

Polymerization of ethylene and propylene has also been monitored by XPS, IR, and Raman spectroscopy [89, 91, 120, 141]. The valence band XPS spectra of polyethylene and polypropylene are characterized by two and three lines between 13 and 19 eV binding energy, respectively. The two outer lines of the polypropylene are due to excitations in methylene groups while the central peak corresponds to methyl group excitations. Subsequent polymerization of propylene and ethylene results in a layered polymer film with polypropylene being at the polymer gas interface and polyethylene being located underneath. From this result in combination with the observation that XPS shows Ti and Cl signals only at the substrate/polymer interface (measured after peeling off the polymer film) it was concluded that polymerization occurs at the solid support [141]. Even though the active site remains at the substrate surface during polymerization, the chemical environment at the catalyst changes during the course of the polymerization.

After polymerization took place an additional EPR signal located at $g = 2.002$ was observed. This signal can be assigned to Ti^{3+} centers within an organic environment [142, 143]. This result points towards a change of the chemical environment of the Ti center at the interface during polymerization. The signal intensity and width varies considerably from preparation to preparation, but there is no simple correlation of these quantities with the activity.

An important characteristic of polypropylene is the tacticity of the material. Kim and Somorjai have investigated the tacticity of the polymer by means of the different solubilities of iso- and atactic polypropylene in boiling *n*-alkanes [120]. The soluble fractions were dried on glass surfaces and investigated by AFM. Based on these results a significant enhancement of isotactic polypropylene was found for catalysts prepared by $TiCl_4$ adsorption on Au as compared to a $MgCl_2$-based system. In fact, Kim et al. claim that the $TiCl_y$/Au catalyst produces exclusively isotactic polypropylene whereas the other catalyst produces a mixture of iso- and atactic polypropylene. It should be noted that an analysis of IR spectra of the grown polymer is not as conclusive. The isotactic index based on the intensity ratio of vibrations at 998 and 973 cm^{-1}, which is used in literature to estimate the amount of isotactic polypropylene (e.g., [144]), is much lower than expected based on the extraction results [120]. The IR analysis might be hampered by amorphous fractions of the polymer. However, values of the isotactic index measured after high temperature treatment to increase the crystallinity of the sample, or independent measurements such as NMR are not available.

Kim and Somorjai have associated the different tacticity of the polymer with the variation of adsorption sites for the two systems as titrated by mesitylene TPD experiments. As discussed above, the $TiCl_y$/Au system shows just one mesitylene desorption peak which was associated with desorption from low coordinated sites, while the $TiCl_x/MgCl_x$ exhibits two peaks assigned to regular and low coordinated sites, respectively [23]. Based on this coincidence, Kim and Somorjai claim that isotactic polymer is produced at the low-coordinated site while atactic polymer is produced at the regular surface site. One has to bear in mind, however, that a variety of assumptions enter this interpretation, which may or may not be valid. Nonetheless it is an interesting and important observation which should be confirmed by further experiments, e.g., structural investigations of the activated catalyst. From these experiments it is clear that the degree of tacticity depends on catalyst preparation and most probably on the surface structure of the catalyst; however, the atomistic correlation between structure and tacticity remains to be clarified.

The kinetics of the reaction has been studied by IR as well as laser reflection interferometry (LRI) [21, 145]. The amount of polymer grown on the surface was measured from the LRI signal as a function of time. It was shown that propylene polymerization was about 30 times slower than ethylene polymerization [145]. In addition, Kim et al. estimated the polymerization ac-

tivity of the model catalyst to be 2–8 times lower that that of commercial catalysts. The observed kinetic was analyzed in terms of a 1st and 2nd order deactivation process, as often used in Ziegler–Natta catalysis [70]. However, transport properties, namely diffusion of the monomers towards the reaction center, can also be responsible for the decrease of the polymerization rate as pointed out by the authors [141].

The course of the reaction has also been studied by evaluating the IR band at 2852 cm^{-1}, which is the one least influenced by the presence of gaseous ethylene [21]. The polymerization has been followed for 12–150 h.

Two different kinds of behavior have been observed. Typical results are given in Fig. 13. The behavior is determined by the degree of disorder in the surface of the model catalyst. While a catalyst with a high degree of disorder shows a monotonous increase of the polyethylene amount with time, catalysts prepared on a smooth and less defected surface show a self-terminating reaction after approximately 50 h leading to a considerably less thick film than in the former case. This can be explained in a straightforward way by considering that on a smooth surface a rather smooth polymer film forms, which becomes impermeable for ethylene from the gas phase in a relatively short period of time so that the reaction is self-limiting. In the other case, the growing film possibly has a sufficient number of pores so that the monomer can continue to reach the catalyst and the reaction keeps going. This assumes that the polymerization reaction takes place at the interface of the polymer and the magnesium chloride support, which has been corroborated experimentally [145]. In the light of these results it seems appropriate to model the kinetic data by assuming diffusion-limited transported of monomer to the interface. The amount of polymer n_e increases with reaction time t according to:

$$n_e = \delta\sqrt{t} \tag{6}$$

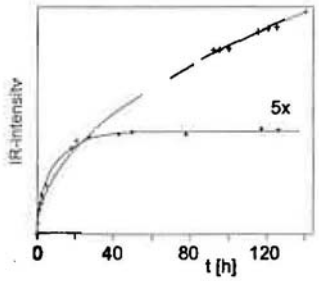

Fig. 13 Amount of polymer as measured by the IR absorption at 2852 cm^{-1} with respect to time. The kinetics observed on a rough catalyst is represented by *crosses*. The *line* through these points is a fit to the kinetic model given in the text. Kinetics observed for smooth catalysts is given by *full circles*. The line is a guide for the eye

where the constant δ is a function of the diffusion coefficient, the surface area, the molar volume of the polymer, and the concentration at infinite time t. Therefore, we expect the IR intensity to increase as $\sqrt{t}$. With $\delta = 4.6 \times 10^{-2} mol\, s^{-1/2}$ the fit given in Fig. 13 has been obtained.

In conclusion, we have shown that the combination of several surface science methods allows a detailed understanding of the properties of surface sites as well as of reactions taking place at the catalyst surface. In particular, EPR spectroscopy has proven useful for elucidating mechanistic details of the activation process of these catalysts.

4 Conclusions

We have reviewed experiments on two classes of systems, namely small metal particles and atoms on oxide surfaces, and Ziegler–Natta model catalysts. We have shown that metal carbonyls prepared in situ by reaction of deposited metal atoms with CO from the gas phase are suitable probes for the environment of the adsorbed metal atoms and thus for the properties of the nucleation site. In addition, examples of the distinct chemical and physical properties of low coordinated metal atoms as compared to regular metal adsorption sites were demonstrated. For the Ziegler–Natta model catalysts it was demonstrated how combination of different surface science methods can help to gain insight into a variety of microscopic properties of surface sites involved in the polymerization reaction.

Acknowledgements We are grateful to all coworkers who have contributed to the results presented here. Their names may be taken from the list of references given below. We would also like to acknowledge support by the Deutsche Forschungsgemeinschaft (SFB 290 and SFB 546), Fond der chemischen Industrie and EU through the TMR project "Oxide surfaces; reactivity of clean and modified oxide surfaces". We are grateful to Dr. Christophe Coperet and Dr. Bruno Chaudret for bringing the work of Negishi et al. to our attention.

References

1. Ertl G, Knözinger H, Weitkamp J (eds) (1997) Handbook of heterogeneous catalysis. Wiley-VCH, Weinheim
2. Gunter PLJ, Niemantsverdriet JWH, Ribeiro FH, Somorjai GA (1997) Catal Rev Sci Eng 39:77
3. Henry CR (1998) Surf Sci Rep 31:235
4. Campbell CT (1997) Surf Sci Rep 27:1
5. Freund H-J (2002) Surf Sci 500:271
6. Libuda J, Freund HJ (2002) J Phys Chem B 106:4901

7. Diebold U (2003) Surf Sci Rep 48:53
8. Freund HJ, Libuda J, Bäumer M, Risse T, Carlsson A (2003) Chem Rec 3:181
9. Poppa H (1993) Catal Rev-Sci Eng 35:359
10. Bäumer M, Freund H-J (1999) Progr Surf Sci 61:127
11. Heiz U, Vanolli F, Trento L, Schneider WD (1997) Rev Sci Inst 68:1986
12. Heiz U, Schneider WD (2000) J Phys D 33:R85
13. Binns C (2001) Surf Sci Rep 44:1
14. Coperet C, Chabanas M, Petroff Saint-Arroman R, Basset JM (2003) Angew Chem Int Ed 42:156
15. Frank M, Bäumer M, Kühnemuth R, Freund H-J (2001) J Phys Chem B 105:8569
16. Frank M, Kühnemuth R, Bäumer M, Freund H-J (2000) Surf Sci 454:968
17. Magg N, Giorgi JB, Frank MM, Immaraporn B, Schroeder T, Bäumer M, Freund H-J (2004) J Am Chem Soc 126:3616
18. Risse T, Carlsson A, Bäumer M, Klüner T, Freund H-J (2003) Surf Sci 546:L829
19. Carlsson AF, Bäumer M, Risse T, Freund H-J (2003) J Chem Phys 119:10885
20. Risse T, Schmidt J, Hamann H, Freund H-J (2002) Angew Chem Intern Ed 41:1517
21. Schmidt J, Risse T, Hamann H, Freund HJ (2002) J Chem Phys 116:10861
22. Magni E, Somorjai GA (1995) Catal Lett 35:205
23. Kim SH, Somorjai GA (2001) Surf Interface Anal 31:701
24. Cox AJ, Louderback JG, Apsel SE, Bloomfield LA (1994) Phys Rev B 49:12295
25. Haruta M (1997) Catal Today 36:153
26. Heiz U, Sanchez A, Abbet S, Schneider W-D (1999) J Am Chem Soc 121:3214
27. Jaeger RM, Kuhlenbeck H, Freund H-J, Wuttig M, Hoffmann W, Franchy R, Ibach H (1991) Surf Sci 259:235
28. Kulawik M, Nilius N, Rust HP, Freund HJ (2003) Phys Rev Lett 91:6101
29. Stierle A, Renner F, Streitel R, Dosch H, Drube W, Cowie BC (2004) Science 303:1652
30. Bäumer M, Frank M, Libuda J, Stempel S, Freund H-J (1997) Surf Sci 391:204
31. Bäumer M, Libuda J, Sandell A, Freund H-J, Graw G, Bertrams T, Neddermeyer H (1995) Ber Bunsenges Phys Chem 99:1381
32. Bäumer M, Frank M, Heemeier M, Kühnemuth R, Stempel S, Freund H-J (2000) Surf Sci 454–456:957
33. Frank M, Bäumer M (2000) Phys Chem Chem Phys 2:3723
34. Frank M, Kühnemuth R, Bäumer M, Freund HJ (1999) Surf Sci 427–428:88
35. Yang AC, Garland CW (1957) J Phys Chem 61:1504
36. Yates JT Jr, Duncan TM, Worley SD, Vaughan RW (1979) J Chem Phys 70:1219
37. Rice CA, Worley SD, Curtis CW, Guin JA, Tarrer AR (1981) J Chem Phys 74:6487
38. Solymosi F, Knoezinger H (1990) J Chem Soc Faraday Trans 86:389
39. Basu P, Panayotov D, Yates JT (1987) J Phys Chem 91:3133
40. Solymosi F, Bansagi T (1993) J Phys Chem 97:10133
41. Hayden BE, King A, Newton MA (1998) Surf Sci 397:306
42. Nilius N, Wallis TM, Ho W (2003) Phys Rev Lett 90:6808
43. Dulaurent O, Chandes K, Bouly C, Bianchi D (1999) J Catal 188:237
44. Tessier D, Rakai A, Bozonverduraz F (1992) J Chem Soc Faraday Trans 88:741
45. Hicks RF, Qi HH, Kooh AB, Fischel LB (1990) J Catal 124:488
46. Rainer DR, Wu MC, Mahon DI, Goodman DW (1996) J Vac Sci Techn A 14:1184
47. Wolter K, Seiferth O, Libuda J, Kuhlenbeck H, Bäumer M, Freund HJ (1998) Surf Sci 402–404:428
48. Wolter K, Seiferth O, Kuhlenbeck H, Bäumer M, Freund H-J (1998) Surf Sci 399:190
49. Papai I, Goursot A, Stamant A, Salahub DR (1992) Theor Chim Acta 84:217
50. Zhou MF, Andrews L, Bauschlicher CW (2001) Chem Rev 101:1931

51. Zhou MF, Andrews L (1999) J Am Chem Soc 121:9171
52. Mineva T, Russo N, Freund HJ (2001) J Phys Chem A 105:10723
53. Bogicevic A, Jennison DR (1999) Phys Rev Lett 82:4050
54. Abbet S, Riedo E, Brune H, Heiz U, Ferrari AM, Giordano L, Pacchioni G (2001) J Am Chem Soc 123:6172
55. Abbet S, Ferrari AM, Giordano L, Pacchioni G, Hakkinen H, Landman U, Heiz U (2002) Surf Sci 514:249
56. Bogicevic A, Jennison DR (2002) Surf Sci 515:L481
57. Toomes RL, King DA (1996) Surf Sci 349:1
58. Beitel GA, Laskov A, Oosterbeek H, Kuipers EW (1996) J Phys Chem 100:12494
59. Bradshaw AM, Pritchard J (1970) Proc Roy Soc Lond A 316:169
60. Heal MJ, Leisegang EC, Torrington RG (1978) J Catal 51:314
61. Gardner RA, Petrucci RH (1960) J Am Chem Soc 82:5051
62. Kavtaradze NN, Sokolova NP (1964) Russ J Phys Chem 38:548
63. Sheppard N, Nguyen TT (1978) In: Hester RE, Clark RJH (eds) Advances in infrared and Raman spectroscopy, vol 5. Heyden, p 67
64. Heemeier M, Carlsson AF, Naschitzki M, Schmal M, Bäumer M, Freund H-J (2002) Angew Chem Intern Ed 41:4073
65. Ziegler K, Holzkamp E, Breil H, Martin H (1955) Angew Chem Int Ed 67:541
66. Natta G, Pino P, Mazzanti P U.S. Patent 3 715 344
67. Natta G (1955) J Polym Sci 16:143
68. Barbé PC, Cecchin G, Noristi L (1987) Adv Polym Sci 81:1
69. Kaminsky W, Arndt M (1997) In: Ertl G, Knözinger H, Weitkamp J (eds) Handbook of heterogeneous catalysis, vol 5. Wiley-VCH, Weinheim, p 2405
70. Dusseault JJA, Hsu CC (1993) J Macromol Sci C 33:103
71. Fink G, Mühlhaupt R, Brintzinger HH (eds) (1995) Ziegler catalysts: recent scientific innovations and technological improvements. Springer, Berlin Heidelberg New York
72. Boor J (1979) Ziegler–Natta catalysts and polymerization. Academic, New York
73. Keii T (1982) Kinetics of Ziegler–Natta polymerization. Chapman & Hall, London
74. Kissin YV (1985) Isospecific polymerization of olefins. Springer, Berlin Heidelberg New York
75. Sinn H, Kaminsky W (1980) Adv Organomet Chem 18:99
76. Pasquon I, Giannini U (1984) In: Anderson JR, Boudart M (eds) Catalysis, science and technology. Springer, Berlin Heidelberg New York, p 65
77. Chien JCW (ed) (1975) Coordination polymerization. Academic, New York
78. Quirk RP (ed) (1988) Transition metal catalyzed polymerization: Ziegler–Natta and metathesis polymerizations. Cambridge University Press, Cambridge
79. Kaminsky W, Sinn H (eds) (1988) Transition metals and organometallics as catalysts for olefin polymerization. Springer, Berlin Heidelberg New York
80. Sinn H (1995) Marcomol Symp 97:27
81. Weiss H, Boero M, Parrinello M (2001) Marcomol Symp 173:137
82. Boero M, Parrinello M, Weiss H, Hüffer S (2001) J Phys Chem 105:5096
83. Martinsky C, Minot C, Ricart JM (2001) Surf Sci 490:237
84. Seth M, Margl PM, Ziegler T (2002) Macromolecules 35:7815
85. Hemmerich I, Rohr F, Seiferth O, Dillmann B, Freund H-J (1997) Z Phys Chem 202:31
86. Thüne PC, Loos J Lemstra PJ, Niemantsverdriet JW (1999) J Catal 183:1
87. Magni E, Somorjai GA (1996) Surf Sci 345:1
88. Magni E, Somorjai GA (1995) Appl Surf Sci 89:187
89. Koranyi TI, Magni E, Somorjai GA (1999) Topics Catal 7:179

90. Magni E, Somorjai GA (1996) J Phys Chem 100:14786
91. Kim SH, Somorjai GA (2000) J Phys Chem B 104:5519
92. Fairbrother DH, Roberts JG, Rizzi S, Somorjai GA (1997) Langmuir 13:2090
93. Fairbrother DH, Roberts JG, Somorjai GA (1998) Surf Sci 399:109
94. Roberts JG, Gierer M, Fairbrother DH, van Hove MA, Somorjai GA (1998) Surf Sci 399:123
95. Rous PJ (1992) Prog Surf Sci 39:3
96. van Hove MA (1997) Surf Rev Lett 4:479
97. Heinz K, Hammer L (1998) Z Kristall 213:615
98. Tasker PW (1984) Adv Ceram 10:176
99. Pankratz LB (1984) Thermodynamic properties of halides. US Dept. of Interior Bureau of Mines, Washington DC
100. Lin JS, Catlow CRA (1993) J Mater Chem 3:1217
101. Guo XC, Hoffman A, Yates JT (1989) J Chem Phys 90:5787
102. Galli P, Barbe P, Guidetti G, Zannetti R, Martorana A, Marigo A, Bergozza M, Fichera A (1983) Eur Polym J 19:19
103. Gerbasi R, Marigo A, Martorana A, Zannetti R, Guidetti GP, Baruzzi G (1984) Eur Polym J 20:967
104. Corradini P, Barone V, Fusco R, Guerra G (1979) Eur Polym J 15:1133
105. Costuas K, Parrinello M (2002) J Phys Chem B 106:4477
106. Magni E, Somorjai GA (1995) Surf Sci 341:L1078
107. Magni E, Somorjai GA (1997) Surf Sci 377:824
108. Schmidt J (2001) Charakterisierung eines Ziegler-Natta-Modellkatalysators für die Polyethylen-Herstellung – Untersuchung mit ESR und IRAS bei der Präparation und Ethylen-Polymerisierung. PhD, Ruhr-Universität Bochum
109. Kinno S, Onaka R (1983) J Phys Soc Jpn 52:267
110. Fryburg GC, Lad RA (1975) Surf Sci 48:353
111. Den Hartog HW, Mollema P, Schaafsma TJ (1973) Phys Status Solidi B 55:721
112. Peyroche J, Girard Y, Laputte R, Guyot A (1969) Makromol Chem 129:215
113. Soga K, Terano M (1981) Macromol Chem Phys 182:2439
114. Zakharov VA, Makhtarulin SI, Poluboyarov VA, Anufrienko VF (1984) Macromol Chem Phys 185:1781
115. Chien JCW, Wu JC (1982) J Polym Sci, Polym Chem Ed 20:2461
116. Fuhrmann H, Herrmann W (1994) Macromol Chem Phys 195:3509
117. Magni E, Somorjai GA (1998) J Phys Chem B 102:8788
118. Kim SH, Tewell CR, Somorjai GA (2000) Langmuir 16:9414
119. Kvisle S, Rytter E (1984) Spectroc Acta Pt A-Molec Biomolec Spectr 40:939
120. Kim SH, Somorjai GA (2001) J Phys Chem B 105:3922
121. Ayscough PB, Thomson C (1962) Trans Faraday Soc 58:1477
122. Morehouse RL, Christiansen JJ, Gordy W (1966) J Chem Phys 45(5):1751
123. Tebbe FN, Parshall GW, Reddy GS (1978) J Am Chem Soc 100:3611
124. Toriyama K, Iwasaki M, Nunome K (1979) J Chem Phys 71(4):1698
125. Schlienz H, Beckendorf M, Katter UJ, Risse T, Freund H-J (1995) Phys Rev Lett 74:761
126. Beermann C, Bestian H (1959) Angew Chem Int Ed 71:618
127. D'yachowvskii FS, Khrushch NE, Shilov AE (1968) Kin Catal (USSR) 9:831
128. de Vries H (1961) Recl Trav Chim Pays-Bas 80:866
129. Negishi E, Kondakov DY, VanHorn DE (1997) Organometallics 16:951
130. Painter PC, Runt J, Coleman MM, Harrison IR (1977) J Polym Sci – Polym Phys Ed 15:1647